Chapter 2
Ultrafast Infrared Plasmonics—A Novel Platform for Spectroscopy and Quantum Control

Satoshi Ashihara and Ikki Morichika

Abstract A marriage of ultrashort-pulsed laser and plasmonics in the mid-infrared range creates a novel platform for light–molecule interactions. Resonant gold nanoantennas are exploited to realize ultrasensitive nonlinear vibrational spectroscopy and vibrationally mediated chemical reaction control. Arbitrary shaping of spatiotemporal field distribution both in nanometer scale and in femtosecond scale has a great promise for advanced vibrational spectroscopy and controlled ground-state chemistry.

2.1 Ultrafast Plasmonics in the Mid-Infrared

2.1.1 Nanoscale Localization of Ultrashort Pulses

An ultrashort laser pulse is characterized by its short temporal duration, wide spectral bandwidth, and high peak power. These features are particularly beneficial for the application of nonlinear spectroscopy, which enables time-resolved measurements of ultrafast processes in atoms, molecules, and solids.

Since the time scale of nuclear motion in molecules and solids is close to or longer than 10 fs (10^{-14} s), ultrashort laser pulses with femtosecond time duration have provided insight into nuclear motions in chemical reactions, opening an innovative field called 'femtochemistry' [1].

Ultrashort laser pulses are useful not only for observing ultrafast processes but also for actively controlling them. Many spectral components with well-defined phase

S. Ashihara (✉) · I. Morichika
Institute of Industrial Science, The University of Tokyo, Meguro-ku, Tokyo, Japan
e-mail: ashihara@iis.u-tokyo.ac.jp

I. Morichika
e-mail: m-ikki@iis.u-tokyo.ac.jp

© Springer Nature Switzerland AG 2021

T. Yatsui (ed.), *Progress in Nanophotonics 6*, Nano-Optics and Nanophotonics,
https://doi.org/10.1007/978-3-030-71516-8_2

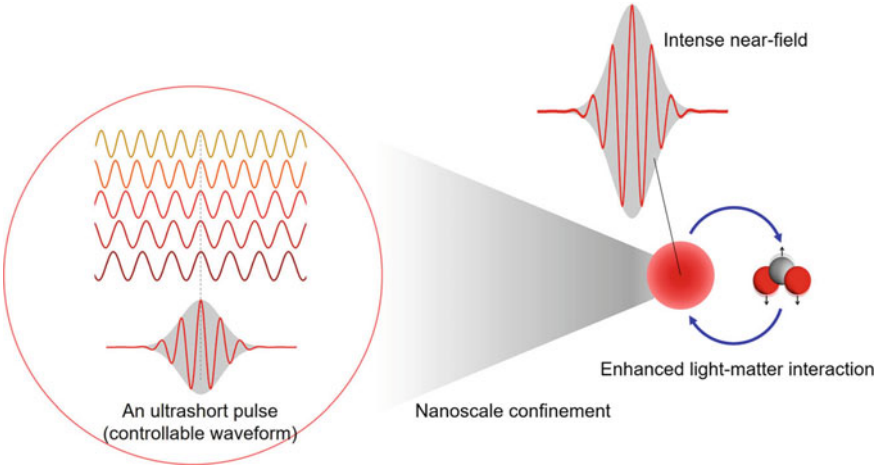

Fig. 2.1 Concept of nanoscale localization of an ultrashort optical pulse

relationships that constitute ultrashort pulses enable coherent excitation of multiple electronic, vibrational, and rotational transitions and manipulation of quantum mechanical interference of transition pathways [2, 3]. Such control over the microscopic behavior of matter, called quantum control, is essential for chemical reaction control and quantum information processing [4–6].

When an ultrashort optical pulse illuminates a metal nanostructure, a surface plasmon is excited, and an intense electromagnetic field, localized both in space and in time, is generated [7] (see Fig. 2.1). Most importantly, the degrees of freedom in the temporal waveform of an ultrashort pulse and the degrees of freedom in the geometrical shape of the nanostructure allow us *to control an electric-field distribution both in nanometer scale and in femtosecond scale* [7–12]. Such spatiotemporally confined and designable fields have great promise for substantial enhancement and precise control of light–matter interactions.

2.1.2 Light–Matter Interaction in the Mid-Infrared Range

An electromagnetic wave in the mid-infrared (mid-IR) range (2 to 20 μm) resonates with a variety of molecular vibrational modes, making it a powerful probe for structural analysis and sensing of chemical species. The most popular type of linear infrared (IR) vibrational spectroscopy is Fourier transform infrared (FT-IR) spectroscopy using a thermal light source.

By utilizing ultrashort mid-IR pulses to exploit nonlinear vibrational spectroscopy, such as pump–probe spectroscopy and two-dimensional spectroscopy, one can resolve ultrafast dynamics of structural changes and vibrational relaxations, as well as

vibrational anharmonic coupling, which cannot be revealed by linear IR spectroscopy [13, 14]. In fact, the structure and dynamics of hydrogen-bonded molecular systems which are deeply involved in life (fluctuating structure of liquid water, folding dynamics of proteins, etc.) have been revealed by nonlinear vibrational spectroscopy [15, 16].

Ultrashort mid-IR pulses enable mode-selective, multi-quantum vibrational excitation with broad accessibility to the potential energy surface. They provide a powerful tool in active control over molecular processes at electronic ground states because the strong excitation of key reagent vibrations directly contributes to selective reaction control [17], as has been validated by theoretical studies [18–21].

However, nonlinear vibrational spectroscopy and vibrational quantum control have suffered from low sensitivity and low efficiency, respectively, mainly due to the small dipole moments of vibrational transitions (they are generally much smaller than those of electronic transitions). In fact, the observation of nonlinear vibrational signals from a small number of molecules or for vibrational modes of smaller transition dipole moments is challenging. In chemical reaction control experiments, multi-quantum vibrational excitation is usually inefficient, especially in condensed phases, and therefore, energy injected into a specific bond does not exceed the potential barrier of the targeted reaction.

2.1.3 A Novel Platform for Vibrational Spectroscopy and Quantum Control

We may resolve these issues via a marriage of ultrafast laser technology and plasmonics in the mid-IR range. Surface plasmon excitation enables subwavelength localization and strong field enhancement of ultrashort mid-IR pulses, which is expected to strengthen the interactions of mid-IR pulses with molecular vibrations, creating a novel platform for nonlinear vibrational spectroscopy and vibrational quantum control.

In recent years, we have studied ultrafast responses and spatial characteristics of surface plasmons in the mid-IR range [22–24] and performed non-destructive measurements of plasmonic near-fields on a femtosecond timescale by using a nonlinear photoemission process at a metal surface [25]. Then, we applied the mid-IR plasmonics to realize enhanced strong-field phenomena at the nanoscale [25, 26], ultrasensitive nonlinear vibrational spectroscopy [27, 28], and vibration-mediated chemical reaction control [29].

2.1.4 Outline

The outline of this chapter is as follows. We describe the basic properties of surface plasmons and metal nanoantennas in the mid-IR range in Sect. 2.2, we describe the measurement of plasmonic near-fields by means of field-driven photoemission in Sect. 2.3, and we present the applications of resonant metal nanoantennas to ultrafast vibrational spectroscopy and chemical reaction control in Sects. 2.4 and 2.5, respectively. We summarize and provide future perspectives in Sect. 2.6.

2.2 Mid-IR Plasmonics

2.2.1 Surface Plasmon Polariton on Gold

Plasmonics in the mid-IR range is gaining increasing attention [30–32] because of promising applications in surface-enhanced spectroscopy [33–39], chemical/biosensing [40, 41], thermal radiation control [42], optoelectronic circuits [43, 44], etc. Surface plasmons may be excited at mid-IR wavelengths on various materials [31, 32], but their properties are different according to the material in which they are excited. In this subsection, we briefly review surface plasmons on gold at mid-IR wavelengths by comparing them with those on a doped semiconductor.

When a slowly varying electric field is applied to a conducting material, free electrons move and thus induce electric polarization in the direction opposite to the external field. This motion is reflected in a large negative real part of the permittivity. When the electric field oscillates at a higher frequency, free electrons do not immediately follow the change in the electric field. As a result, the absolute value of the permittivity decreases. This motion of free electrons and the resultant change in permittivity govern the frequency-dependent characteristics of surface plasmons.

Figure 2.2 shows the dispersion relationship of surface plasmon polaritons (SPPs) propagating along the interface between gold and air (red line) at a frequency below 100 THz or a wavelength above 3 μm (the Drude parameters are taken from [45]). As seen in the inset of Fig. 2.2, the dispersion relation bends strongly in the visible range as the frequency approaches the plasma frequency of gold. The decreased slope of the dispersion curve indicates that the phase velocity and wavelength decrease (that is, wavelength compression occurs). In contrast, the dispersion curve is close to the light line (gray dashed line) in the near- and mid-IR ranges, which indicates that the phase velocity is close to that of free-space light in air.

Figure 2.3a shows the calculated penetration depth of the electromagnetic field of an SPP into air, δ_d, normalized by the free-space wavelength λ_0. The electromagnetic field of the SPP is localized within the subwavelength dimension from the interface in the visible range, whereas it penetrates into air with a dimension much larger than λ_0 in the mid-IR range. Figure 2.3b shows the calculated propagation length

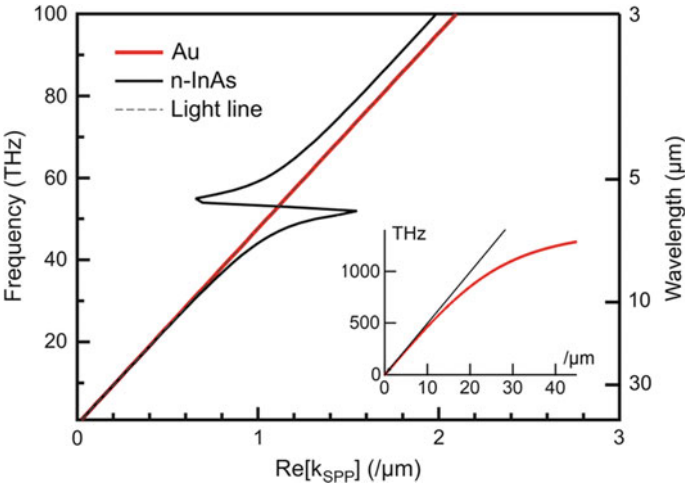

Fig. 2.2 Dispersion curve of SPP propagating along Au/air interface [45] (*red line*) and that of SPP propagating along *n*-InAs/air interface [46] (*black line*). A light line is shown as *gray dashed line*

L_{SPP} normalized by λ_0. We can see that the propagation length increases with the operation wavelength, exceeding 10^3 times the free-space wavelength λ_0.

As mentioned above, SPPs behave differently depending on the operation wavelength. In the visible range, the electromagnetic field is strongly bound to the interface, the wavelength compression is remarkable, and the propagation distance is short. In the near- and mid-IR ranges, the electromagnetic field is only weakly bound to the interface, the wavelength compression is subtle, and the propagation distance is long.

To obtain subwavelength mode confinement in the mid-IR range, materials with plasma frequencies in the mid-IR range should be exploited. As an example, we display in Fig. 2.2a a dispersion curve of *n*-doped InAs with a plasma frequency of 5.5 μm [46]. The dispersion curve bends at mid-IR wavelengths of 6–10 μm, indicating wavelength compression at these wavelengths. The penetration depth δ_{SPP} is smaller than the free-space wavelength λ_0, as shown in Fig. 2.3a, meaning that subwavelength confinement can be achieved in the mid-IR range. However, there is a cost of substantially reduced propagation length L_{SPP} as shown in Fig. 2.3b.

A good reference to the achievable electric-field enhancement is a figure of merit (FOM) defined as $M = L_{SPP}/\delta_{SPP}$, which provides a clear illustration of the confinement/propagation length trade-off [32]. As we see from Fig. 2.3a, b, gold exhibits a much larger FOM than *n*-InAs at mid-IR wavelengths. As this comparison shows, noble metals are generally more suited for applications in which a small loss, long propagation length, or large electric-field enhancement is required in the mid-IR range than materials that have plasma frequencies in a lower frequency range. Although the noble metals of silver and copper display very similar SPP properties, gold is an excellent plasmonic material because of its superior chemical stability [47].

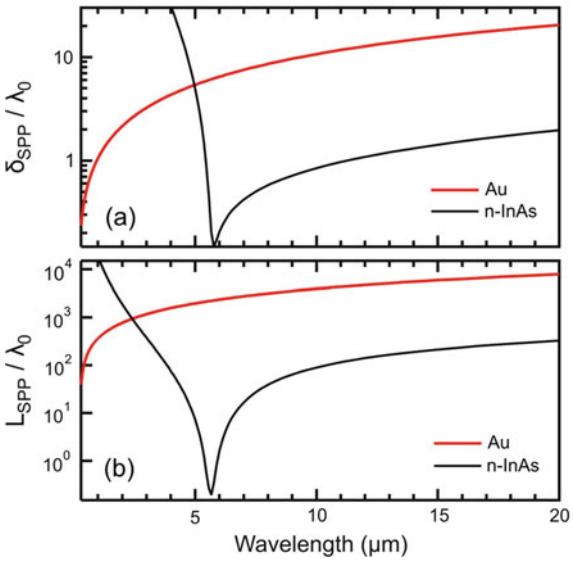

Fig. 2.3 **a** Penetration depth of the SPP into air (normalized to the free-space wavelength λ_0) at Au/air interface (*red*) and at *n*-InAs/air interface (*black*). **b** Propagation length (normalized to λ_0) of SPP at Au/air interface (*red*) and at *n*-InAs/air interface (*black*)

2.2.2 Gold Nanoantennas

Metal nanorods serve as dipole antennas in the visible and IR ranges. They may be viewed as plasmonic cavities where SPPs form stationary or eigenmodes. Therefore, the resonance frequency may be tailored by adjusting the size, shape, and dielectric properties of the nanorod. When a nanorod is resonantly excited, the electromagnetic field is significantly enhanced near the nanorod ends. This electric-field enhancement is useful for strengthening light–matter interactions, especially nonlinear processes that increase nonlinearly with the field strength.

In applying plasmonic near-field enhancements to nonlinear spectroscopy and quantum control where ultrashort pulses are exploited, not only the magnitude of electric-field enhancement but also its temporal/spectral response is important. In this subsection, we describe the spectral properties of near-field enhancement obtainable with gold nanorods, which resonate at mid-IR frequencies [22].

Figure 2.4 displays a typical electric-field distribution or field enhancement factor for a resonantly excited gold nanorod (1250 nm in length) on a ZnS substrate, as calculated by using the finite difference time-domain (FDTD) method. The electric field is substantially enhanced near the nanorod ends in a dimension much smaller than the free-space wavelength.

Electric-field enhancement at a frequency ν is expressed with a transfer function defined as $H(\nu) = E_{\mathrm{lo}}(\nu)/E_{\mathrm{in}}(\nu)$, where $E_{\mathrm{in}}(\nu)$ and $E_{\mathrm{lo}}(\nu)$ denote the complex electric-field amplitude of the incident light and the enhanced near-field, respectively. Correspondingly, the intensity enhancement factor and the enhancement phase are defined as $\eta(\nu) = |H(\nu)|^2$ and $\phi(\nu) = \arg H(\nu)$, respectively.

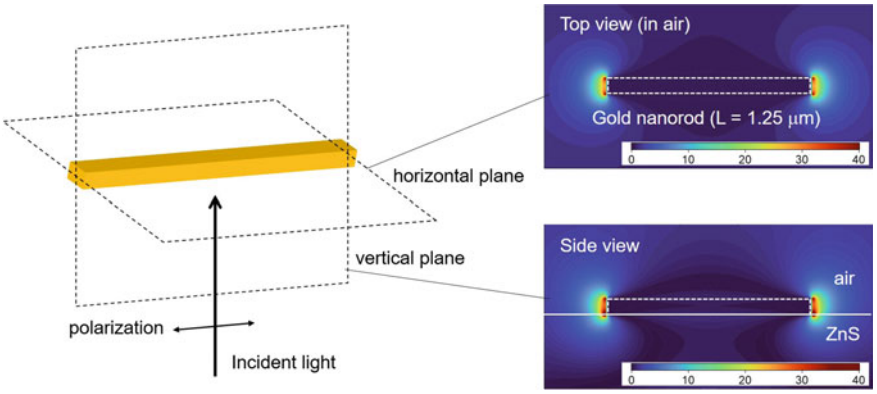

Fig. 2.4 Simulated near-field distribution at each of the horizontal and vertical cross sections when a gold nanorod with a length of 1.25 μm on a ZnS substrate is resonantly excited

The intensity enhancement factor $\eta(\nu)$ at a position near the nanorod tip is displayed in Fig. 2.5a for gold nanorods with varied lengths ($L = 1000, 1250, 1750,$ and 2500 nm) and a common width (thickness) of 100 nm (100 nm) [22]. Here, we estimate $H(\nu)$ for the electric-field component parallel to the nanorod long axis. Each nanorod exhibits near-field enhancement at its resonant frequency, and the enhancement factor at resonance ranges from 300 to 1500.

Figure 2.5b shows the extinction cross section of the gold nanorod obtained from the transmission measurement performed with an FT-IR spectrometer [22]. Here, gold nanorods with the same dimensions as those used in simulations are fabricated on a ZnS substrate. The transmission is measured for the polarization parallel to the nanorod long axis using a polarizer. A typical scanning electron micrograph of a nanorod is shown in the inset. Each nanorod exhibits resonant behavior in the extinction in the same fashion as in the field enhancement. The slight difference in the peak position and the spectral profile between the field enhancement (near-field spectrum) and the extinction (far-field spectrum) is attributed to a general feature of damped harmonic oscillators [48].

Interestingly, Fig. 2.5a, b show that the linewidth $\Delta\nu$ is linearly proportional to the resonance frequency ν_0 of the antenna. This means that the quality factor $\Delta\nu/\nu_0$ of the plasmonic cavity is nearly constant for the nanorods resonating at mid-IR frequencies. This frequency dependence of the linewidth, $\Delta\nu \propto \nu_0$, is explained as the nature of radiation loss (see [22] for details). Since the electromagnetic field of a surface plasmon on gold is only weakly bound to the interface in the mid-IR range, Joule heating loss is suppressed so that damping of the antenna mode is dominated by radiation loss.

For an incidence of an ultrashort pulse, the spectrum of the enhanced near-field may be squeezed and its temporal waveform may be stretched owing to the finite bandwidth of the near-field enhancement. Figure 2.6a shows the enhancement factor $\eta(\nu)$ and the phase $\phi(\nu)$ for a gold nanorod with a length of 1000 nm. The maximum

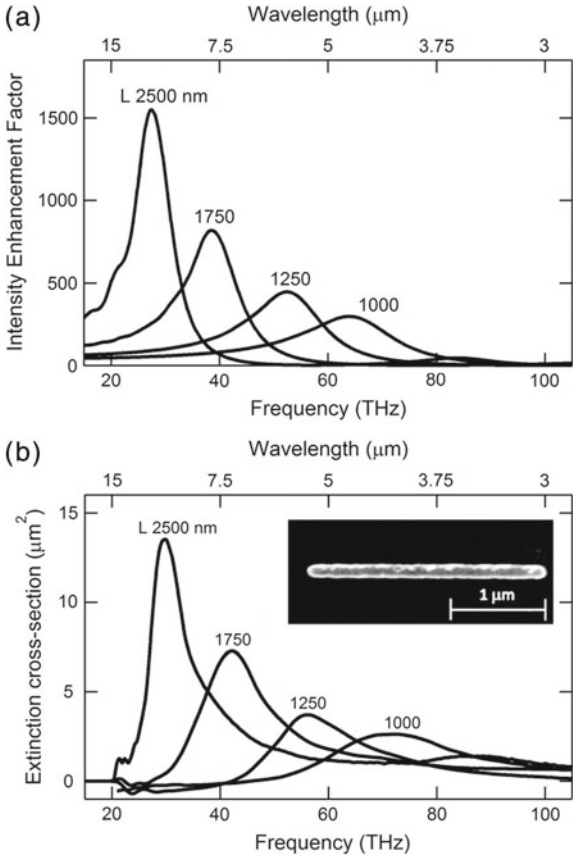

Fig. 2.5 **a** Calculated intensity enhancement factors near the nanorod end and **b** the measured extinction cross sections for nanorods of different lengths. The inset in **b** shows a scanning electron micrograph of a fabricated nanorod. These figures are reprinted with permission from [22]. Copyright ©2014, American Institute of Physics

enhancement is reached at 5 μm and the phase changes from 0 to π across the resonance. For reference, the power spectrum of a 100-fs pulse (dashed line) and that of a 30-fs pulse (dotted line) are also shown in Fig. 2.6a. The frequency spread of the enhancement $\eta(\nu)$ is sufficiently larger than the spectral width of the 100-fs pulse, and the phase ϕ can be approximated as a straight line throughout its pulse spectrum. In contrast, the frequency spread of $\eta(\nu)$ is approximately the same as the spectral width of the 30-fs pulse, and the phase ϕ can no longer be regarded as a straight line.

Figure 2.6b displays the temporal waveform of the enhanced near-field for incident pulses with a duration of 100 fs (upper panel) and 30 fs (lower panel). Here, the incident waveform is shown as a dashed line. For the 100-fs incident pulse, the enhanced near-field faithfully follows the incident waveform except for a phase shift of approximately $\pi/2$. For the 30-fs incident pulse (corresponding to two optical cycles), the enhanced near-field is elongated in time with respect to the incident field. From a series of simulations, we find that near-field enhancement is achieved

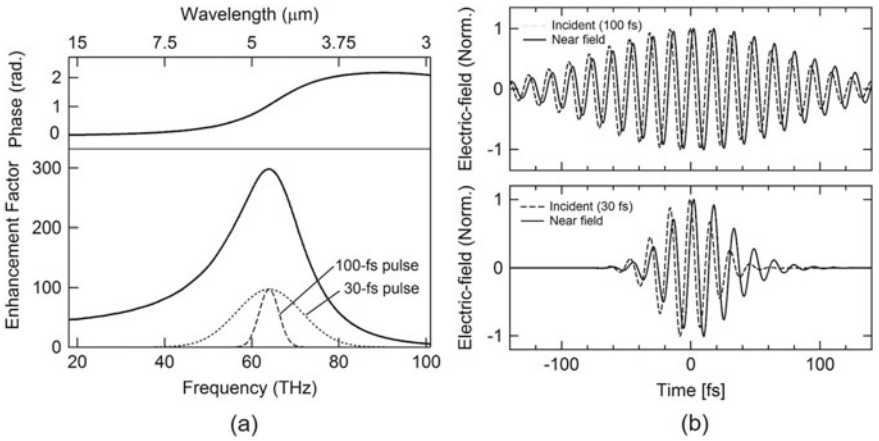

Fig. 2.6 **a** Calculated intensity enhancement factor (*lower panel*) and phase (*upper panel*) for a 1000-nm-long gold nanorod. Power spectra for a 100-fs pulse and a 30-fs pulse are shown as *dashed* and *dotted lines*, respectively. **b** Temporal waveform of the incident electric field (*dashed*) and the enhanced near-field (*solid*) for an incident pulse duration of 100 fs (*upper panel*) and 30 fs (*lower panel*). These figures are reprinted with permission from [22]. Copyright ©2014, American Institute of Physics

with high fidelity in the temporal waveform if the incident pulse contains at least three optical cycles in its envelope [22].

2.3 Measurement of Plasmonic Near-Field Using Field-Driven Photoemission

In this section, we discuss the emission of an electron from gold nanorods driven by mid-IR pulses [25]. Upon resonant excitation of gold nanorods, the enhanced near-field created near the nanorod ends modifies the potential so that free electrons in gold may be emitted via quantum mechanical tunneling (see Fig. 2.7). Because the tunneling current exhibits characteristic dependence on the local electric field, it is possible to extract local field strength from intensity-dependent tunneling current measurements. Such quantitative information on the plasmonic near-field is of immediate relevance for antenna-enhanced nonlinear vibrational spectroscopy and antenna-enhanced quantum control, which will be described in the following sections.

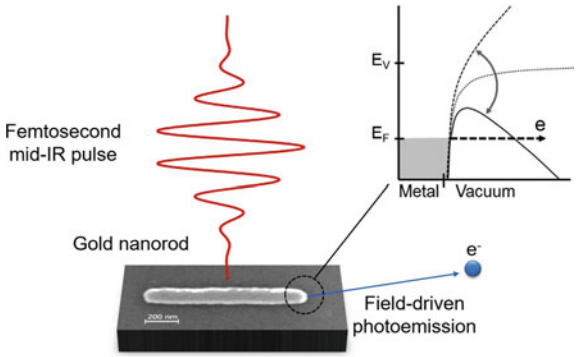

Fig. 2.7 Schematic of field-driven photoemission from a gold nanorod. A free electron in a gold nanorod may be emitted via quantum mechanical tunneling because of a modification of a potential induced by a plasmonic near-field of a mid-IR pulse

2.3.1 Field-Driven Photoemission

Strong-field light–matter interaction at surfaces and nanostructures has been intensively studied to date, with special focus on local field enhancements and subwavelength confinement of optical fields. Nonlinear photoelectron emission has been studied for various metallic nanostructures [49–59], with motivations for ultrafast electron [60–62] and X-ray sources [63], phase-resolved imaging and spectroscopy [64, 65], etc.

Metal nanotips, displaying broadband near-field enhancements, exhibit a representative model system for nonlinear photoelectron emission and acceleration [49, 51, 54, 64, 66]. Nanoparticles and plasmonic antennas, exhibiting field enhancements from surface plasmon resonance and geometric edge enhancement, constitute another platform for photoemission studies [55–57, 59].

When a metal is illuminated by light with a photon energy larger than the work function of the metal, conducting electrons inside the metal can be emitted (photoelectric effect). Even if the photon energy is smaller than the work function, electrons may be emitted via multiphoton absorption or via quantum mechanical tunneling if the illuminating light is intense enough [67]. In the former mechanism, the electron emission rate follows the power-law scaling reflecting the multiphoton process. In the tunneling mechanism, the emission rate follows the physics of quantum mechanical tunneling as we describe later, and interestingly, electron emission occurs within a half cycle of a driving optical pulse [67].

Nonlinear photoemission is well described by the multiphoton mechanism at a lower intensity of $\gamma > 1$ and by the tunneling mechanism at a higher intensity of $\gamma < 1$ [68]. Here, γ is a Keldysh parameter defined as

$$\gamma = \sqrt{\frac{\phi}{2U_p}}, \tag{2.1}$$

where ϕ is a metal work function and $U_p = e^2F^2/(4m\omega^2)$ is ponderomotive energy (e and m are the electron charge and mass, respectively). As we can see, the Keldysh parameter γ is proportional to the optical frequency ω and inversely proportional to the electric field amplitude F. Here, we see that mid-IR pulses provide higher ponderomotive energies and therefore enable access to the strong-field regime at reduced local intensities [54, 58], compared with visible pulses.

2.3.2 Nonlinear Photoemission Experiments

A gold nanorod 1 μm in length, 150 nm in width, and 50 nm in height is patterned into two-dimensional arrays on a ZnS substrate, as shown in Fig. 2.8a, by using electron beam lithography and a lift-off process. Here, the near-field coupling between neighboring nanorods is prevented by a spacing of 5 μm. A 5-nm-thick gold capping serves as a conduction layer to avoid sample charge-up during photoemission.

Mid-IR pulses at center wavelengths tunable from 3–10 μm and pulse durations of approximately 160 fs are produced at a 1 kHz repetition rate by parametric down conversion of amplified Ti:sapphire laser pulses. A parabolic mirror is used to focus the mid-IR pulses to spot diameters of approximately 30 μm. To illuminate multiple rods (approximately 8000), the sample is placed at a defocus position with a beam diameter of approximately 500 μm, giving rise to incident peak intensities of 0.5–1.5 GW/cm^2 for pulse energies of 80–230 nJ. The excitation linear polarization is set to be parallel to the nanorod axis, and we excite a fundamental longitudinal mode or the half-wave dipole antenna mode that has a resonance wavelength of 5 μm. The emitted photoelectrons are guided by a magnetic bottle to a time-of-flight (TOF) spectrometer for measuring photoelectron yields and kinetic energy spectra.

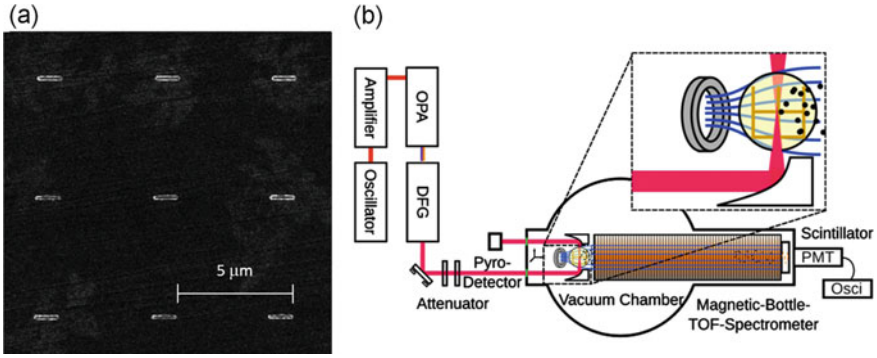

Fig. 2.8 **a** Scanning electron micrograph of a nanorod array (rod length 1 μm). **b** Experimental setup. Tunable mid-IR pulses are focused onto a nanorod array in a high vacuum chamber. Electron kinetic energy spectra are measured with a magnetic-bottle time-of-flight spectrometer. These figures are reprinted with permission from [25]. Copyright ©2015, American Institute of Physics

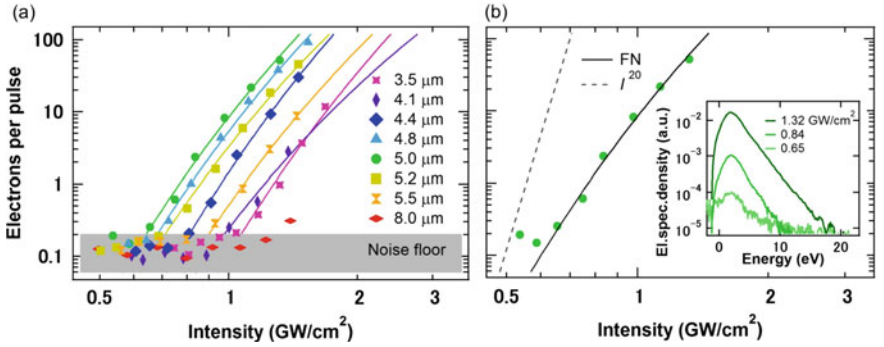

Fig. 2.9 **a** Electron yield for different excitation wavelengths as a function of incident intensity. Each curve is fitted by Fowler–Nordheim equation (*solid line*) to extract the intensity enhancement factor. **b** Fowler–Nordheim fit to the electron yield at 5 μm wavelength (*solid line*). For comparison, a corresponding multiphoton dependence (*dashed line*, slope 20) is shown. Inset: Electron kinetic energy spectra for selected intensities. These figures are reprinted with permission from [25]. Copyright ©2015, American Institute of Physics

The photoelectron yield is displayed as a function of incident peak intensity for varied excitation wavelengths in Fig. 2.9a. All curves exhibit a strongly nonlinear intensity dependence. We also find that the curves for excitation wavelengths closer to the antenna resonance reside at lower intensity, which indicates *the underlying near-field enhancement*.

Under the static-field approximation, the tunnel current density J generated by an electric field F at the metal surface is given by the Fowler–Nordheim (FN) equation [69]

$$J = \frac{e^3 E^2}{16\pi^2 \hbar \phi} \exp\left(-\frac{4\sqrt{2m_e}\phi^{3/2}}{3\hbar F}\right), \tag{2.2}$$

where m_e and $\hbar$ denote the electron effective mass and Dirac constant, respectively. To characterize the photoemission regime and to evaluate local field enhancement, the intensity dependence of the electron yield is analyzed by fitting with the FN equation, as shown in Fig. 2.9 (solid lines). Note that we use the modified FN equation that includes barrier reduction or the Schottky effect [70].

Throughout the measured intensity range, the nonlinearity of the yield (or the local slope in the double logarithmistic plot) is smaller than the corresponding multiphoton dependence (slope 20 at a photon energy of 0.25 eV and the 5.1 eV work function) and decreases with intensity. From the FN fits, we extract a local electric-field amplitude of 3.5 Vnm^{-1} and a Keldysh parameter γ of approximately 0.80, which indicates field-driven or tunneling photoemission as the underlying mechanism. The kinetic energy spectra of photoelectrons measured for varied incident intensities at 5 μm excitation are displayed in inset of Fig. 2.9b. We find that the kinetic energy cutoff (when defined to include 99% of the electron population) linearly increases with intensity, consistent with ponderomotive scaling [71].

2.3.3 Estimation of Plasmonic Near-Field

Fig. 2.10a displays the measured far-field extinction spectrum of the nanorod arrays, which exhibit a resonance at a wavelength of 5 μm. Figure 2.10b displays the photoelectron yield measured for different excitation wavelengths at a constant incident intensity of 1.1 GW/cm^2 (triangles). The photoelectron yield peaks at 5 μm, indicating that the observed photoemission is governed by the resonantly enhanced near-field. The intensity enhancement factor obtained from the FN fits to the electron yields is plotted as circles in Fig. 2.10b, where we find a maximum intensity enhancement factor of 1290 and the corresponding maximum field enhancement factor of 36. The photoelectron yield exhibits much sharper resonance profile compared with the underlying near-field, which is reasonably understood as a result of the high nonlinearity of the emission process.

To support the experimental results, the electromagnetic field distribution is numerically calculated with the FDTD method [22]. Here, the nanorods are modeled with the experimental dimensions (length: 1 μm, height: 50 nm, width: 150 nm), as shown in the inset of Fig. 2.10c. The simulated far-field extinction shown in Fig. 2.10c agrees well with the experiment, exhibiting an asymmetric resonance at 5 μm with a linewidth of 21 THz. The inset in Fig. 2.10c shows the spatial distribution of the electric-field component parallel to the nanorod axis for 5 μm excitation. The inten-

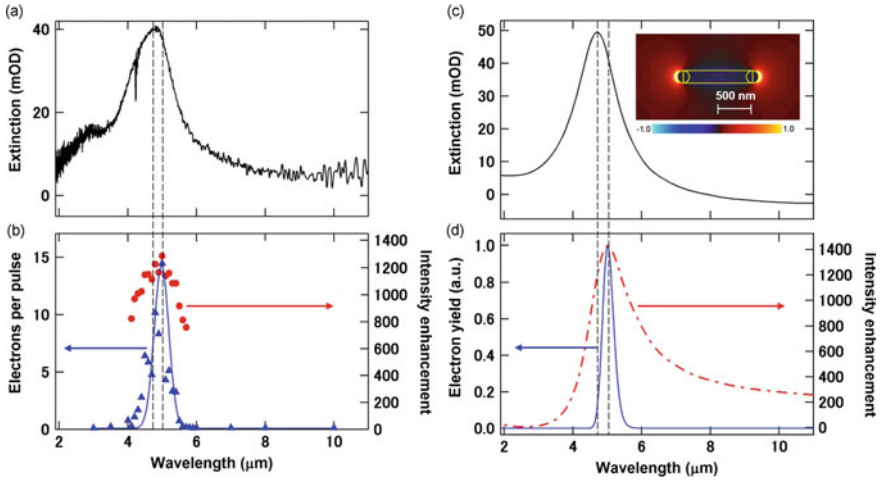

Fig. 2.10 **a** Measured far-field extinction spectrum. **b** Experimental photoemission yield as a function of excitation wavelength and for constant incident intensity (*triangles*) and intensity enhancement factors extracted from the corresponding yield curves (*circles*). **c** Simulated far-field extinction spectrum for 1 μm long nanorods. The inset shows the electric-field distribution for the component parallel to the nanorod. **d** Simulated local intensity enhancement factor (*dashed-dotted line*) and electron yield (*solid line*) as a function of the excitation wavelength. Dashed vertical lines indicate a redshift of spectral near-field enhancement relative to the far-field extinction spectrum. These figures are reprinted with permission from [25]. Copyright ©2015, American Institute of Physics

sity enhancement factor at the position of the largest electric field is shown as a dashed-dotted line in Fig. 2.10d. Here, we find that the maximum value of approximately 1400 agrees well with the experimental value. The solid line represents the photoelectron yield calculated with the FN equation. It exhibits a narrowed width of 5 THz, in agreement with the experimental value of approximately 6 THz.

In both the experiment and the simulations, the near-field enhancement is highest at a slightly red-shifted wavelength compared to the far-field extinction spectrum (see vertical dashed lines in Fig. 2.10a–d. In the experiments presented above, such spectral shifts between near- and far-field spectra, universal to damped harmonic oscillators [48, 72], are successfully observed by using the nonlinear photoemission process as a noninvasive probe.

2.3.4 Summary on Field-Driven Photoemission

Field-driven photoemission is successfully demonstrated with resonant gold nanorods excited by femtosecond mid-IR pulses. The wavelength-dependent, nonlinear photoelectron yield follows the resonance profile of the nanorods, and intensity-dependent measurements allow for a noninvasive determination of the local intensity (field) enhancement factor well exceeding 1000 (30).

2.4 Antenna-Enhanced Nonlinear Infrared Spectroscopy

Mid-IR ultrashort lasers have enabled nonlinear vibrational spectroscopy, which is a powerful, label-free technique providing direct insight into the molecular structures and dynamics. Unfortunately, the widespread use of these techniques is severely limited by low sensitivity due to the weak interaction of molecular vibrations with IR radiation. An attractive way to amplify the light–molecule interaction is the use of plasmonic field enhancements. Recently, we utilized periodically arranged IR-resonant nanoantennas in pump-probe spectroscopy and achieved a local signal enhancement of more than 6 orders of magnitude, substantially reducing the required pump energy from the micro-joule to the nano-joule level [27]. Furthermore, we have demonstrated the reflection type of antenna-enhanced nonlinear spectroscopy, which is useful for surface-selective measurements [28]. In this section, we will review the historical perspective of such plasmon-enhanced IR spectroscopy and then present our experimental results and considerations.

2.4.1 *Vibrational Spectroscopy with Infrared Ultrashort Lasers*

The mid-IR range of the spectrum corresponds to energies associated with molecular vibrations (Fig. 2.11). Since the vibrational properties are directly linked to the molecular constituents, their chemical bonds, and their configuration, the mid-IR absorption spectra, often referred to as molecular fingerprints, provide a vast amount of structural information about molecules.

In the last quarter century, the advent of mid-IR ultrashort laser techniques has enabled nonlinear vibrational spectroscopy, such as IR pump-probe spectroscopy and two-dimensional infrared (2D-IR) spectroscopy, which provides richer information than is available from linear spectroscopy [13, 14]. In IR pump-probe spectroscopy, ultrashort pulse sequences are used to excite and detect molecular vibrations, enabling time-resolved study of the molecular dynamics on the timescales on which they actually occur (typically femtosecond to picosecond timescales for elementary steps in chemical reactions) [1]. In 2D-IR spectroscopy, mid-IR absorption spectra are spread into two frequency dimensions, providing information on vibrational couplings, spectral diffusion, and chemical exchange.

Despite their fascinating potential, however, the applications of nonlinear vibrational spectroscopy are somewhat limited due to the small absorption cross sections of molecular vibrations ($\sigma_{abs} \approx 10^{-20}\text{cm}^2$). The experiments require mid-IR pump pulses of the micro-joule level, typically generated by the complex frequency conversion system based on the regenerative amplifier. Even if the mid-IR pulses of the micro-joule level are exploited, nonlinear signals can be observed for only a limited number of vibrational modes whose absorption cross sections are relatively large (e.g., CO, NH, OH stretching vibrations). These facts severely limit the widespread use of the nonlinear vibrational spectroscopy.

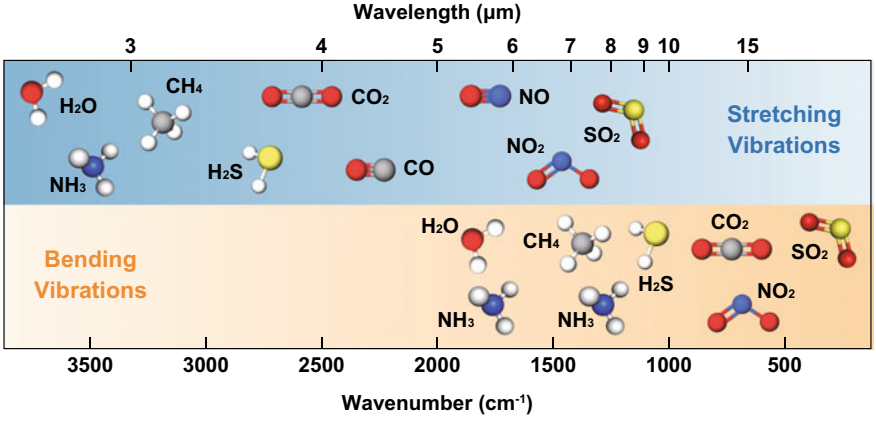

Fig. 2.11 Characteristic molecular vibrations in the mid-infrared range

2.4.2 Surface-Enhanced Infrared Absorption Spectroscopy

One promising approach to overcome the limitations described in the previous subsection is to amplify the interaction of molecular vibrations with IR light utilizing surface plasmon excitation. As described in Sect. 2.2, plasmonics take advantage of the coupling of light to metal electrons, enabling subwavelength localization and strong field enhancements. Therefore, surface plasmon excitation substantially enhances the light–matter interactions.

For linear IR spectroscopy, this concept was first applied in 1980 by Hartstein and coworkers [33]. They demonstrated that linear vibrational signals of molecules adsorbed on randomly arranged Ag nanoparticles (with plasmonic resonances located in the visible spectral range) were enhanced by a factor of 20. This phenomenon, which was later named surface-enhanced infrared absorption (SEIRA), is currently commonly used in various applications such as electrochemistry and biosensing [39, 41].

A significantly stronger enhancement can be obtained by using well-defined metallic nanostructures whose plasmonic resonances are tuned to the respective molecular vibration. This approach of resonant SEIRA was first demonstrated in 2008 by Neubrech and coworkers [34]. They achieved the detection of 50 attograms of molecules located in the plasmonic hot-spots of a nanoantenna and found that the vibrational signals are enhanced by 5 orders of magnitude. In the following years, along with significant advances in nanofabrication technologies, numerous SEIRA morphologies have been proposed and demonstrated to substantially enhance the vibrational signals for an expanding range of applications[37, 38].

Plasmonic near-field enhancement is expected to be useful for amplifying nonlinear vibrational signals as well. In fact, the benefits of near-field enhancement are expected to be larger for nonlinear spectroscopy because nonlinear signals increase superlinearly with field strength. In 2013, Donaldson et al. first applied near-field enhancement to nonlinear IR spectroscopy [73]. They demonstrated 2D-IR spectroscopy on capping layers of gold nanoparticles with off-resonant plasmonic responses and found that the nonlinear signals were enhanced by 2 orders of magnitude. Later, Selig et al. performed pump-probe and 2D-IR spectroscopies of 5 nm polymer layers on randomly arranged IR-resonant nanoantennas and observed a nonlinear signal enhancement of 4 orders of magnitude [74].

2.4.3 Near-Field Enhancements by Diffractively Coupled Nanoantenna Arrays

An obvious way to further increase the sensitivity is to use nanostructures providing higher field enhancements. Near-field enhancement can be improved by optimizing not only the geometries of the individual nanoantennas but also their arrangements. Nanoantenna arrays arranged in a certain period scatter incident light to produce

diffracted waves. When one of the diffracted waves propagates in the plane of the array, it may couple the plasmonic resonances associated with individual nanoantennas. In such diffractive coupling conditions, the diffracted waves act to counter the radiation damping of the single nanoantenna response, leading to significant improvements in field enhancement well beyond what is achievable by simply tuning their geometries [75].

In view of applying diffractive coupling to enhanced ultrafast spectroscopy, we investigate the spectral/temporal properties of plasmonic near-fields with FDTD-based numerical simulations. In our simulations, the dimensions of each nanoantenna (length: 1200 nm, width: 200 nm, height: 30 nm) and the arrangement period along the longer axis ($d_x = 2.0$ μm) are fixed, whereas the arrangement period along the shorter axis d_y is varied (Fig. 2.12a).

The calculated field enhancement spectra for varied d_y show crests along the diffractive coupling condition of $d_c = m(\lambda/n)$, where m is a positive integer, λ is the wavelength, and n is the refractive index of the substrate (Fig. 2.12b). Although the isolated nanoantenna exhibits a peak enhancement of 40 at 2000 cm^{-1} and a fwhm bandwidth of 560 cm^{-1}, the nanoantenna arrays of $d_y = 3.2$ μm (nearly the diffractive coupling condition) exhibit a larger peak enhancement of 80 and a narrower bandwidth of 180 cm^{-1} (Fig. 2.12c).

Figure 2.12d shows the temporal waveforms of the incident electric field of 100-fs duration, the enhanced near-field for the isolated nanoantenna, and that for the nanoantenna arrays of $d_y = 3.2$ μm. The peak electric field is found to be enhanced by 40 times for the isolated nanoantenna and 70 times for the nanoantenna arrays. Such a large enhancement is accompanied by a slight elongation of the temporal duration (120 fs for the isolated nanoantenna and 140 fs for the nanoantenna arrays) due to the spectral filtering effect.

From these results, we can conclude that diffractive coupling is beneficial for higher field enhancements and thus higher sensitivity but sacrifices the time resolution and the available bandwidth. In practice, one should choose adequate d_y to balance the magnitude and bandwidth of the field enhancement, according to the required time resolution (the typical time scale for condensed-phase molecular dynamics varies from tens of femtoseconds to tens of picoseconds).

2.4.4 Linear Spectroscopy of Antenna–Molecule System

Rod-shaped gold nanoantenna arrays are patterned into 2D arrays of rectangular lattices ($d_x = 1.9$ μm, $d_y = 3.3$ μm) on a CaF_2 substrate, whose SEM image is shown in the inset of Fig. 2.13a. On this device, a $W(CO)_6$-dispersed PMMA film of 80-nm thickness is formed. Our target mode is the triply degenerate anti-symmetric CO stretching vibration (T_{1u} mode) of $W(CO)_6$.

As shown in the upper panel of Fig. 2.13a, the extinction spectrum for the polymer film deposited directly on a CaF_2 substrate has two absorption peaks (fwhm bandwidth) at 1976 cm^{-1} (19 cm^{-1}) for the T_{1u} mode of $W(CO)_6$ and at 1731 cm^{-1} (14

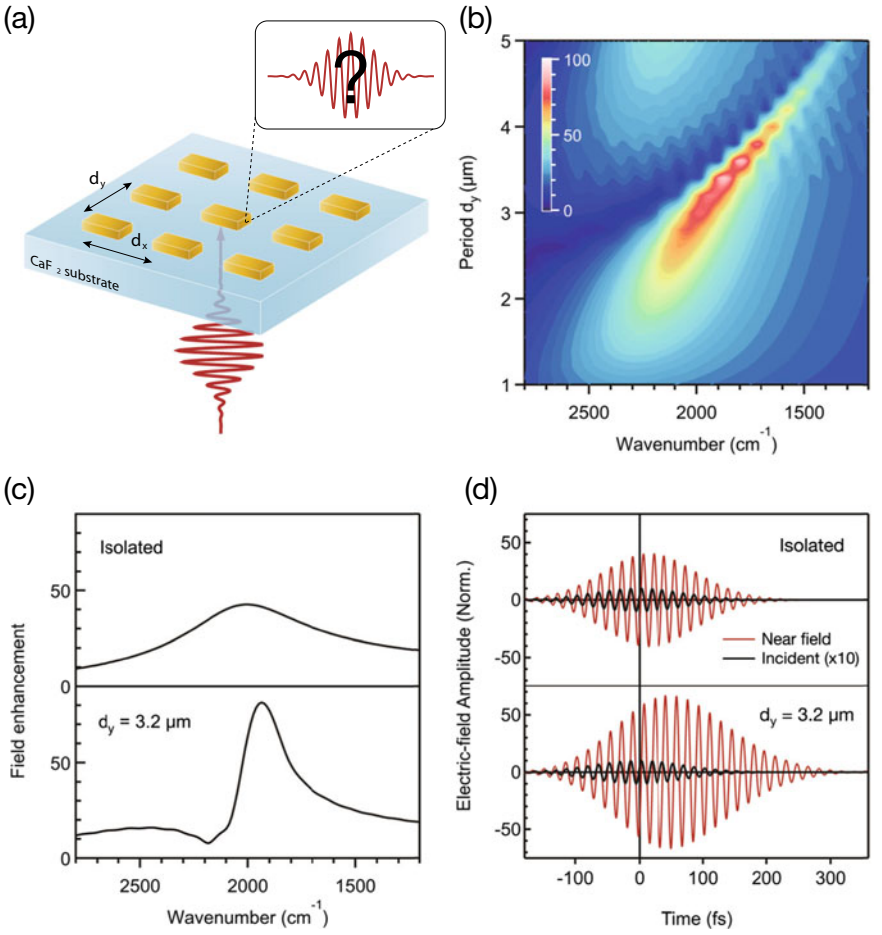

Fig. 2.12 **a** Sketch of the nanoantenna arrays in the numerical simulations. **b** Calculated field enhancement of gold nanoantenna arrays for varied d_y. **c** Field enhancement spectra for $d_y = 3.2$ μm and infinity (isolated). **d** Temporal waveforms of the incident electric field of 100-fs duration, enhanced near-fields for the isolated nanoantenna and for the nanoantenna arrays of $d_y = 3.2$ μm. Adapted from [27]. Copyright ©2017, OSA Publishing

cm^{-1}) for the CO stretching mode of PMMA. In contrast, the extinction spectrum for the polymer film deposited on the nanoantenna arrays (the lower panel in Fig. 2.13a) shows that the broad peak of the plasmonic resonance is modulated at the resonance frequencies of the two vibrational modes, with spectral features characteristic of Fano resonance.

These features are caused by coupling to the molecular vibration in the following manner (see Fig. 2.13b). The incident field excites the plasmon mode (process I), which in turn excites the molecular vibration via near-field coupling (process

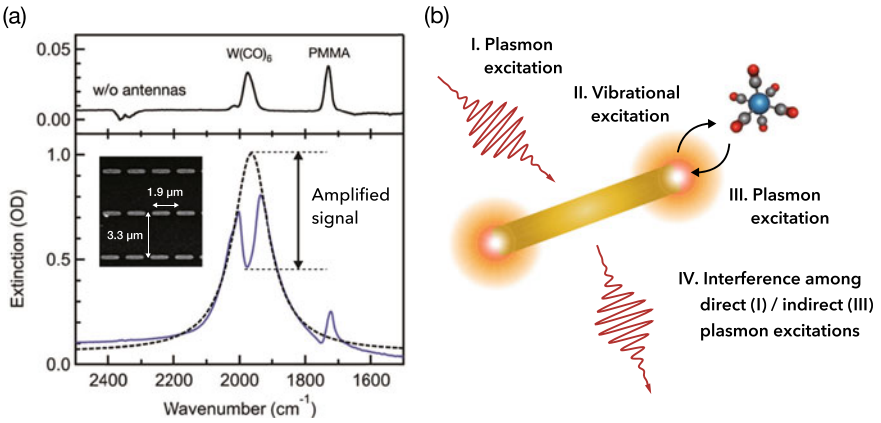

Fig. 2.13 **a** The *upper panel* shows the extinction spectrum for the 80-nm-thick $W(CO)_6$:PMMA film deposited directly on a CaF_2 substrate. The *lower panel* shows that for the diffractively coupled nanoantenna arrays covered (*solid line*) and uncovered (*dashed line*) with the polymer film. The SEM image of the nanoantennas is shown in the *inset*. Each nanoantenna is 1.45 μm long, 0.2 μm wide, and 0.03 μm high. The size of the array unit cell is 1.9 μm × 3.3 μm. **b** Schematic of the antenna-molecule near-field coupling. Adapted from [27]. Copyright ©2017, OSA Publishing

II). Next, the molecular vibrational excitation acts back to excite the plasmon mode (process III). In this manner, coherent dipole excitation is continuously exchanged between the nanoantenna and the molecules until it is damped. Consequently, the modification in the antenna extinction, resulting from such interference among direct/indirect plasmon excitations (process IV), corresponds to the amplified vibrational signal [76, 77].

2.4.5 *Pump-Probe Spectroscopy of Antenna–Molecule System*

We perform single-color IR pump-probe spectroscopy for the T_{1u} mode of $W(CO)_6$ using the setup described in [27]. The spectra of the pump and probe pulses are centered at 2000 cm^{-1} with a fwhm bandwidth of 180 cm^{-1}. The time resolution of the pump-probe measurements is approximately 100 fs.

Figure 2.14c shows the transient absorbance change spectra at scanned delay times for the $W(CO)_6$-dispersed PMMA film without nanoantennas, measured with a pump energy of 890 nJ. Bleaching at the fundamental transition frequency and induced absorption at the red-shifted frequency appear immediately after excitation and decay monotonically. The bleaching signal is attributed to population depletion of the $v = 0$ ground state and stimulated emission from the $v = 1$ state. The induced absorption at the red-shifted frequency is attributed to excited-state absorption of the $v = 1 \rightarrow 2$ transition.

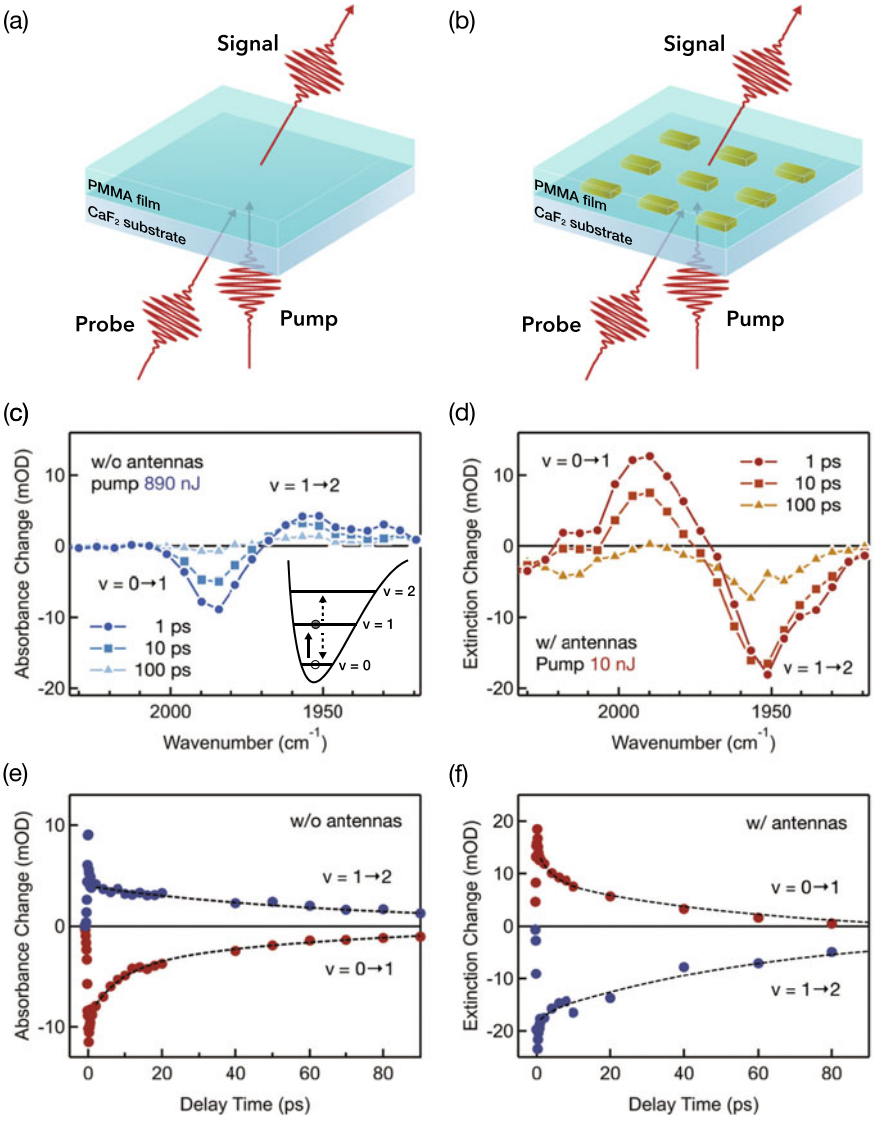

Fig. 2.14 **a**, **b** Schematics of the pump-probe spectroscopy for the $W(CO)_6$-dispersed PMMA film (**a**) without the nanoantennas and (**b**) with the nanoantennas. **c**, **d** Transient extinction change spectra at scanned delay times for the $W(CO)_6$-dispersed PMMA film **c** without the nanoantennas and **d** with the nanoantennas. **e**, **f** Delay scans for the $W(CO)_6$-dispersed PMMA film **e** without the nanoantennas and **f** with the nanoantennas. Adapted from [27]. Copyright ©2017, OSA Publishing

Figure 2.14d shows the transient extinction change spectra at scanned delay times for the $W(CO)_6$-dispersed PMMA film with nanoantennas, measured with a pump energy of 10 nJ. The transient extinction changes display similar behaviors as the typical pump-probe absorbance changes, except for their signs. The inversion of the signs is reasonably explained by the observation of molecular vibrational signals through Fano-like resonant interactions with nanoantennas (Fig. 2.13a). Then, the increased extinction around the fundamental transition frequency is attributed to ground-state bleach($v = 0 \rightarrow 1$) and stimulated emission($v = 1 \rightarrow 0$), whereas the decreased extinction at the red-shifted frequency is attributed to the excited-state absorption($v = 1 \rightarrow 2$).

One can find that the transient extinction changes are comparable between the two measurements shown in Fig. 2.14c, d, despite different pump energies of 890 nJ and 10 nJ, respectively. This indicates that the nonlinear vibrational signal is substantially amplified by the near-field enhancement. From these results, the "spatially-averaged" nonlinear signal enhancement factor, calculated as the extinction change divided by pump energy and then normalized by its value for the bare sample, is estimated to be 850. Furthermore, by assuming that the signals come from only the hot spots near the extremities of the nanoantennas, the "local" nonlinear signal enhancement factor is estimated to be 6 orders of magnitude.

Figure 2.14e, f show the kinetic data at the probe frequencies of bleach (red circle) and induced absorption (blue circle) for the $W(CO)_6$-dispersed PMMA film with/without the nanoantennas, respectively. The global fitting analyses extract almost identical relaxation times of 60–70 ps for the two cases. This fact indicates that antenna–molecule near-field coupling enables nonlinear vibrational spectroscopy with substantially increased signal sensitivity and only minor modifications to molecular vibrational dynamics.

2.4.6 Summary

We have demonstrated surface-enhanced nonlinear vibrational spectroscopy using diffractively coupled gold nanoantenna arrays. The IR pump-probe spectroscopy measurements on a $W(CO)_6$-dispersed PMMA film elucidate that the diffractive coupling condition achieves a local signal enhancement of more than 6 orders of magnitude. Furthermore, the observed vibrational dynamics are almost identical regardless of the signal enhancements by nanoantenna arrays.

Such substantial signal enhancement should be useful for characterizing the structures and dynamics of minute-volume molecules and for the detection of vibrational modes with smaller transition moments. The demonstrated scheme reduces the required pump energy from the micro-joule to the nano-joule level, paving the way for nonlinear vibrational spectroscopy measurements with compact light sources at the oscillator level [78–80]. Such simplification of the whole system is a critical key for nonlinear vibrational spectroscopy to become widely used. Additionally, the

oscillator-level pulsed sources generate pulses at higher repetition rates, which is advantageous for shorter data acquisition times.

Reflection geometry, combined with strong field confinement, discards the background signal originating from the bulk, enabling surface-sensitive measurements [28, 81, 82]. Therefore, the reflection-type method is useful for investigating monolayers and interfaces, which are important in the field of structural biology, photocatalysis, and organic electronics.

Further engineering in the metal nanostructure is promising for even higher sensitivity and new functionality. Examples of structures that could provide exceptionally high field enhancements are nanogap structures and perfect-absorber metamaterials [83]. Recently, Chuntonov and coworkers employed plasmonic gap trimers, which have two orthogonal dipole resonances, and demonstrated significant enhancement of the cross-peak signal in dual-frequency 2D-IR spectroscopy [84, 85].

2.5 Reaction Control via Antenna-Enhanced Vibrational Excitation

Mid-IR ultrashort lasers have great potential not only for nonlinear vibrational spectroscopy but also for active control of chemical reactions at the molecular level [86]. Deposition of sufficient vibrational energy into a specific chemical bond via IR laser excitation can lead to selective bond cleavage while leaving the surrounding molecules undisturbed. Such molecular surgery has been achieved for gas-phase molecules [87–89], yet attempts at realizing it in condensed phases, which are essential for practical chemical synthesis, have been hampered so far by poor vibrational excitation efficiency [90–93]. Recently, we utilized the plasmonic field enhancement of mid-IR pulses to strongly drive molecular vibrations and thereby realized bond-breaking of condensed-phase molecules for the first time [29] (Fig. 2.15). This section reviews the historical perspective of vibrationally mediated reaction control and our experimental results.

2.5.1 Vibrational Control of Chemical Reactions

Many chemical reactions are driven by thermal activation at the electronic ground state. In such thermally driven reactions, the induced thermal energy populates molecular vibrations participating in the reaction coordinate (RC) and thus propels the reactants over the activation energy barrier to the products. However, heating the molecules results in the excitation of all vibrational modes according to the Boltzmann distribution, which promotes not only desired reactions but also undesired reactions.

Strong excitation of key reagent vibrations is a potentially powerful strategy for bond-selective control of chemical reactions. Upon direct excitation of the RC or by energy relaxation into the RC with vibrational energy above the activation energy barrier, a specific reaction can be promoted while minimizing unwanted side products. Vibrational motions can be activated through electronic excitation, but this scheme is restricted to modes accessible by Franck–Condon transitions and excited-state conical intersections. In contrast, IR excitation of molecular vibrations in electronic ground states may be a more versatile technique because of its much broader accessibility to the potential energy surface.

Mid-IR ultrafast laser pulses have enabled multi-quantum vibrational excitation or vibrational ladder climbing (VLC) and thus opened a way to bond-selective control of chemical reactions in the electronic ground states. Molecular bond-breaking mediated by VLC has been realized for gas-phase molecules [87–89], and similar VLC has been performed on liquid-phase molecules as well [90–93]. Down-chirping has proven useful for efficient VLC [89, 90, 92], and arbitrary pulse-shaping was exploited for selective populations of excited vibrational levels [93]. However, attempts to control ground-state molecular dissociation in liquid phases have been unsuccessful to date because rapid vibrational relaxation disturbs the deposition of sufficient energy in a specific mode [90–93].

One promising approach to resolve these issues is to combine ultrafast laser technology with plasmonics in the mid-IR range. As described in Sect. 2.2, plasmonics takes advantage of the coupling of light to metal electrons, enabling subwavelength localization and strong field enhancements and enhanced light–matter interactions. Since VLC is a higher order nonlinear process, the plasmonic field enhancement may play a key role in accelerating VLC to enable sufficient energy deposition on a timescale faster than vibrational relaxation.

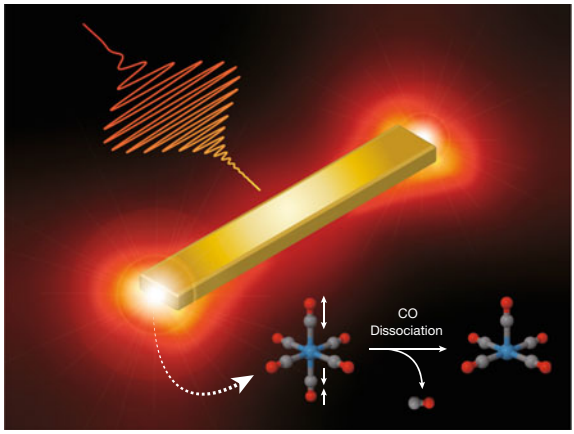

Fig. 2.15 Schematic of reaction control via antenna-enhanced vibrational excitation. The down-chirped mid-IR pulse, enhanced with plasmon excitation of the gold nanoantenna, strongly excites the carbonyl stretch vibration of $W(CO)_6$ molecules, resulting in dissociation of the W-C bond. Adapted from [29]. Copyright ©2019, Nature Publishing Group

2.5.2 *Vibrational Ladder Climbing with Down-Chirped Pulses*

As described above, laser excitation of molecules into a specific higher lying vibrational state is a controllable way to accelerate a desired reaction. Direct excitation of such a higher lying state by single-photon absorption is inefficient because of the small transition dipole moment between the initial and final state. Thus, stepwise excitation of a sequence of vibrational states is a more promising route. Indeed, these transition frequencies decrease while climbing the ladder due to the molecular anharmonicity. Therefore, the climbing efficiency can be increased dramatically when using a negatively chirped pulse so that its high-frequency components, in reso-

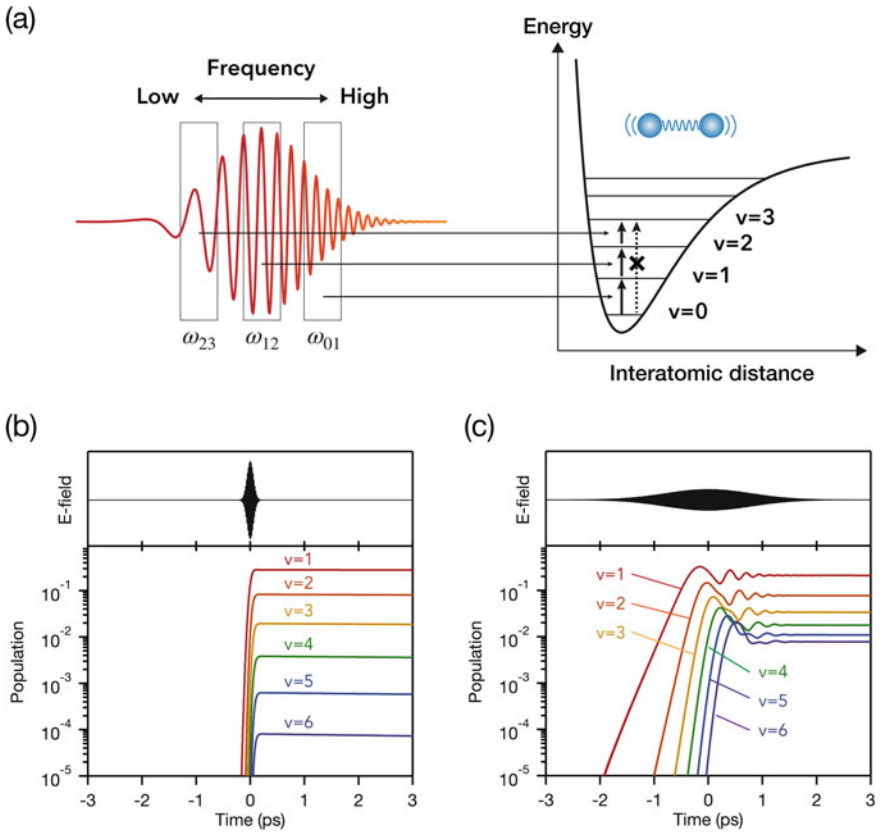

Fig. 2.16 **a** A schematic of vibrational ladder climbing by a down-chirped pulse. **b**, **c** Calculated time evolution of vibrational populations (**b**) for FTL pulse excitation and **c** for down-chirped pulse excitations. The respective electric-field waveforms of the incident pulses are represented in the *upper panels*

nance with the lower transitions of the ladder, precede its low-frequency components, in resonance with the upper transitions of the ladder (Fig. 2.16a).

Figure 2.16b, c show the calculated time evolution of vibrational populations of the T_{1u} CO stretching mode of $W(CO)_6$ excited by Fourier transform limited (FTL) and down-chirped (the group delay dispersion of -24000 fs^2) pulses, respectively (see Supplementary Information of [29] for the detailed description of the calculations). In the case of FTL pulse excitation, the vibrational populations grow simultaneously within the pulse duration. On the other hand, in the case of down-chirped pulse excitation, the vibrational population grows sequentially, resulting in efficiently raising the vibrational population up to the higher lying states.

2.5.3 Antenna-Enhanced Vibrational Ladder Climbing

Our sample is a $W(CO)_6$/*n*-hexane solution held between two CaF_2 windows (Fig. 2.17a). The target mode is the T_{1u} CO stretching mode of $W(CO)_6$, which exhibits an absorption at a center frequency of 1983 cm^{-1} with a fwhm linewidth of 3 cm^{-1} (black line in Fig. 2.17c). The gold nanoantenna arrays are fabricated on one of the two CaF_2 windows, whose SEM image is shown in Fig. 2.17b. The reflectance spectrum for the sample in Fig. 2.17c shows the broad peak of the plasmonic resonance, strongly modified at the resonance frequency of the T_{1u} mode with spectral features characteristic of Fano resonance (see Sect. 2.4.4 for a description of its mechanism).

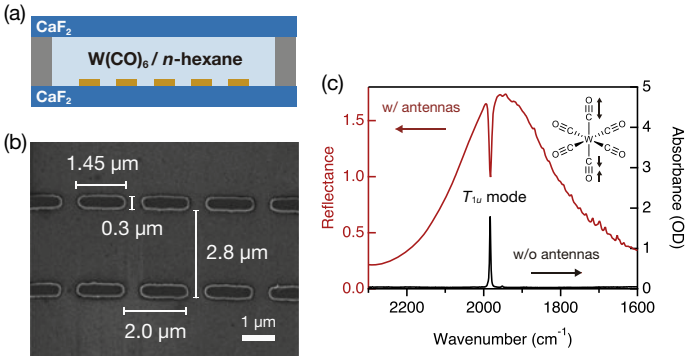

Fig. 2.17 **a** A schematic of the sample comprising two CaF_2 windows separated by a Teflon spacer and filled with $W(CO)_6$/*n*-hexane solution. **b** SEM image of the gold nanoantenna arrays. Each nanoantenna is 1.45 μm long, 0.3 μm wide, and 0.1 μm high. The size of the array unit cell is 2.0 μm × 2.8 μm. **c** The measured reflectance for the nanoantenna arrays immersed in 20 mM $W(CO)_6$/*n*-hexane solution (*red*) and the absorption spectrum for 3 mM $W(CO)_6$/*n*-hexane solution (*black*). These figures are reprinted with permission from [29]. Copyright ©2019, Nature Publishing Group

We perform mid-IR pump-probe spectroscopy for our sample to probe VLC in the T_{1u} mode using mid-IR pulses with a temporal duration of 100 fs and a center frequency of 1930 cm^{-1}. In our experiments, mid-IR pump pulses are locally enhanced with plasmon excitation to strongly drive the T_{1u} mode, and the resulting vibrational population distribution is sensitively probed as the pump-induced reflectance changes.

As a reference experiment, we measure the transient absorption of the uncoupled $W(CO)_6$/*n*-hexane solution (3 mM) in a transmission geometry using nearly FTL pump pulses with a fluence of 0.2 mJ/cm^2. The transient absorbance change of the uncoupled molecules in Fig. 2.18a shows a negative absorption feature at the fundamental T_{1u} mode frequency (1982 cm^{-1}), attributed to the ground-state bleach ($v = 0 \rightarrow 1$) and the stimulated emission ($v = 1 \rightarrow 0$). They also exhibit a positive absorption feature at 1967 cm^{-1}, attributed to the excited-state absorption ($v = 1 \rightarrow 2$).

Next, we measure the transient reflectance of the antenna-coupled $W(CO)_6$/*n*-hexane solution (20 mM) in a reflection geometry using nearly FTL pump pulses with a fluence of 0.2 mJ/cm^2. The transient reflectance change of the antenna-coupled molecules in Fig. 2.18b shows a positive reflectance change at 1982 cm^{-1}, attributed to the ground-state bleach ($v = 0 \rightarrow 1$) and the stimulated emission ($v = 1 \rightarrow 0$). They also exhibit negative reflectance changes, attributed to the excited-state absorptions: $v = 1 \rightarrow 2$ at 1967 cm^{-1}, $v = 2 \rightarrow 3$ at 1953 cm^{-1}, $v = 3 \rightarrow 4$ at 1931 cm^{-1}, $v = 4 \rightarrow 5$ at 1908 cm^{-1}, and $v = 5 \rightarrow 6$ at 1889 cm^{-1}. When the pump pulses are down-chirped with the group delay dispersion of -24000 fs^2, we observe an additional signal at 1866 cm^{-1}, attributed to the excited-state absorption of the $v = 6 \rightarrow 7$ transition (Fig. 2.18c).

From these results, it can be reasonably concluded that the near-field enhancement as well as the down-chirping of the mid-IR pump pulses plays essential roles in realizing VLC up to as high as $v = 6$. Remarkably, this vibrational energy is close to the dissociation energy of one W-C bond. This suggests that the multiphoton excitation energy can be channeled into the W-C bond via intramolecular mode-coupling, resulting in dissociation of a CO ligand.

2.5.4 CO Dissociation Induced by Chirp-Pulsed Near-Fields

We continuously measure the transient reflectance of the antenna-coupled molecules for an hour while irradiating the down-chirped pump pulses. Figure 2.19a shows the transient reflectance change measured before and after an hour of pump irradiation. Surprisingly, the 1 h of irradiation induces a change in the transient reflectance; i.e., there emerges an additional positive signal in the spectral range of 1910–1950 cm^{-1}. From the transient spectrum for 60 min, subtracted by the one for 0 min, it is clearly observed that the new band exhibits a center frequency of 1930 cm^{-1} and a fwhm linewidth of 22 cm^{-1}.

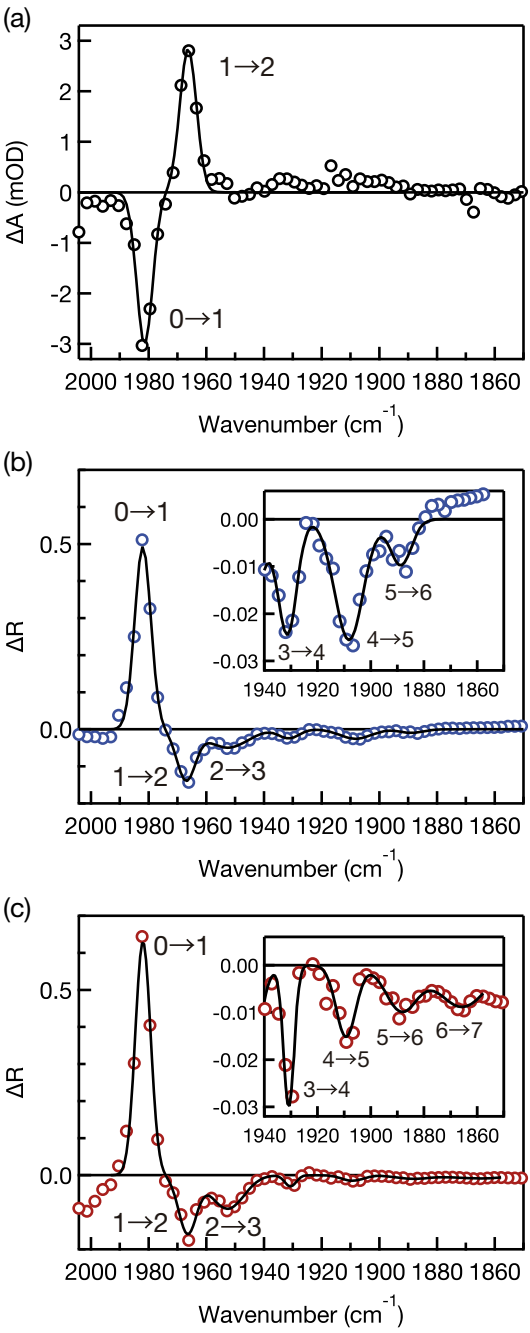

Fig. 2.18 **a** The transient absorbance change of uncoupled $W(CO)_6$ at a 2-ps time delay after excitation with nearly FTL pulses. **b**, **c** The transient reflectance change of coupled $W(CO)_6$ at a 2-ps time delay after excitation: **b** with nearly FTL pulses, and **c** with down-chirped pulses. Each *black line* represents a linear combination of multiple Gaussian functions fitted to the measured absorbance/reflectance change. These figures are reprinted with permission from [29]. Copyright ©2019, Nature Publishing Group

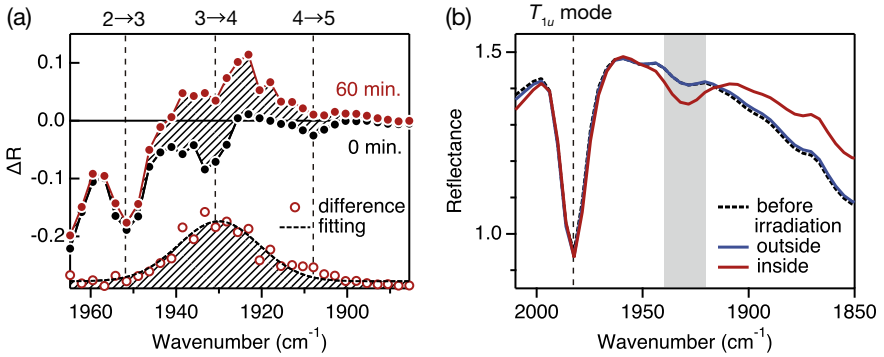

Fig. 2.19 **a** Transient reflectance change at a 2-ps time delay for the antenna-coupled $W(CO)_6$ before (*black filled markers*) and after (*red filled markers*) the 1 h of irradiation. The *red open markers* represent the difference between the two reflectance changes, and the *black dashed line* represents a Gaussian function fitted to the data. **b** The linear reflectance spectrum measured after 1 h of repeated irradiation for the area inside (*red*) and outside (*blue*) the irradiation beam spot. A *black dashed line* denotes the spectrum measured before irradiation. These figures are reprinted with permission from [29]. Copyright ©2019, Nature Publishing Group

After the 1 h of irradiation with the down-chirped pump pulses, we measure the linear reflectance with FT-IR microscope for the sample area inside/outside the irradiation beam spot, as shown in Fig. 2.19b. In addition to the original absorption dip of the T_{1u} mode at 1982 cm^{-1}, an additional absorption dip is observed for the area inside the irradiation beam spot (not observed for the area outside the beam spot). Importantly, this dip exhibits the same center frequency and linewidth as the positive signal observed in the transient reflectance change with the pump irradiation. This coincidence indicates that the newly appearing pump-probe signal shown in Fig. 2.19a originates from the ground-state bleach and the stimulated emission of the vibrational mode with its fundamental resonance at 1930 cm^{-1}.

Spatial localization of the additional band within the irradiation beam spot suggests that it originates from adsorbates, i.e., CO or $W(CO)_5$ adsorbed on the gold surfaces. According to our theoretical calculations based on density functional theory, $W(CO)_5$ becomes stabilized when adsorbed on the gold surface, and the fundamental transition frequency for the A_1 mode of adsorbed $W(CO)_5$ is red-shifted by 45 cm^{-1} compared with that of the T_{1u} mode of $W(CO)_6$. This frequency shift agrees well with the value of 53 cm^{-1} observed in our experiments. From these results, we assign the absorption band observed at 1930 cm^{-1} to the A_1 CO stretching mode of $W(CO)_5$ adsorbed on the gold surface (Fig. 2.20).

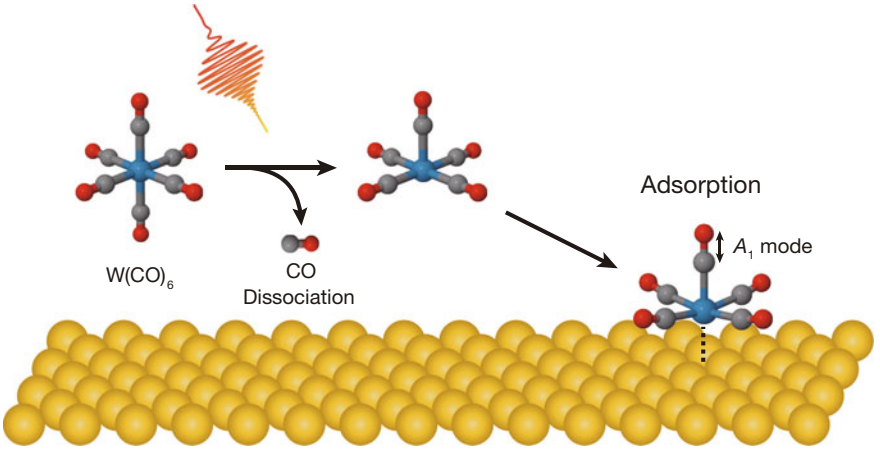

Fig. 2.20 Proposed reaction schemes induced by antenna-enhanced vibrational ladder climbing. Upon multiphoton vibrational excitation, the $W(CO)_6$ molecule loses one CO ligand. CO dissociation is followed by adsorption on the gold surface. This figure is reprinted with permission from [29]. Copyright ©2019, Nature Publishing Group

2.5.5 Summary

We have demonstrated successful driving of ground-state dissociation of liquid-phase molecules by employing plasmonic near-fields of chirped mid-IR pulses. Both down-chirping and plasmonic field enhancement play essential roles in raising vibrational populations to higher lying states, realizing bond dissociation. Interestingly, the gold nanoantennas play an additional role in stabilizing the dissociated species prior to recombination. These key roles solve the long-standing issues of poor excitation efficiency and diffusional recombination that have hampered vibration-mediated dissociation of condensed-phase molecules.

The demonstrated scheme should be useful for mode-selective control of not only bond-breaking but also other kinds of chemical reactions. For instance, Heyne and coworkers have recently demonstrated the acceleration of bimolecular reaction, the alcoholysis of urethane, by exciting a vibrational mode of the reactants [94]. Weinstein and coworkers have achieved mode-specific control of the path of light-induced electron transfer at a molecular fork via vibrational excitation [95].

Our scheme can be developed into more powerful and versatile techniques by incorporating arbitrary pulse-shaping, well-designed plasmonic nanostructures, and functions of metal surfaces, paving the way toward controlled ground-state chemistry.

2.6 Summary and Prospects

As presented in the preceding sections, gold nanoantennas efficiently couple femtosecond mid-IR laser pulses into plasmonic near-fields to substantially enhance ultrafast light–matter interaction at the nanoscale. And thus, these gold nanoantennas have brought about ultrasensitivity onto nonlinear vibrational spectroscopy (Sect. 2.4), and have realized an vibrationally mediated chemical reaction control in a liquid phase (Sect. 2.5). These successful demonstrations illustrate that *ultrafast mid-IR plasmonics form a novel platform for vibrational spectroscopy and vibrational quantum control*, allowing us to view future prospects from several angles.

Substantial signal enhancement in nonlinear vibrational spectroscopy, including 2D-IR spectroscopy, will enable detailed analyses on protein conformations with fewer number of molecules to greatly benefit protein science and biochemistry [16].

Engineering in the metal nanostructure is promising for increased sensitivity and new functionality. For instance, nanogap structures and perfect-absorber metamaterials provide exceptionally high field enhancement [83], whereas plasmonic gap trimers provide a new degree in polarization control of near-fields that allows sequential excitation of multiple vibrational modes whose transition dipole moments may have different orientations [84, 85].

Near-field enhancement at a surface brings about another benefit of *surface sensitivity* to spectroscopy. Especially, antenna-enhanced spectroscopy exploiting reflection geometry (described in Sect. 2.4) provides better surface sensitivity and therefore would be suited for the investigation of monolayers and interfaces, which are important in the field of structural biology, electrochemistry and organic electronics [81]. Although gold and other noble metals exhibit superior field enhancement, the plasmonic near-fields are only weakly bound to metal surfaces. For improved surface sensitivity, other materials with plasma frequencies in the mid-IR range are preferable. Promising candidates are silicides (NiSi and TiSi), doped semiconductors (Si, Ge, and InAs), and graphene [32]. Graphene offers tunable plasma frequency in the mid-IR to THz ranges and strong subwavelength confinement due to its unique band structure [96, 97].

Another benefit of signal enhancement is the reduction in the required pulse energy from the micro-joule to the nano-joule level, which paves the way for nonlinear vibrational spectroscopy measurements with compact light sources of oscillator level, typically operated at the MHz repetition rate [78–80]. This will shorten the acquisition time as well as improve the signal-to-noise ratio to accelerate the wide use of nonlinear vibrational spectroscopy.

The quantum control scheme demonstrated in Sect. 2.5 will be useful for selective control of various kinds of chemical reactions, including an intramolecular bond-breaking reaction, a bimolecular reaction of the alcoholysis of urethane [94], controlled electron transfer at a molecular fork [95], etc. The scheme can be developed into more powerful and versatile techniques by incorporating engineered plasmonic nanostructures, arbitrary pulse-shaping, and functions of metal surfaces, making innovative advance in the long-standing dream of controlled ground-state chemistry.

In parallel to these plasmon-enhanced nonlinear vibrational processes, ultrafast plasmonics play essential roles in the emerging field of strong-field nanoscale science [98, 99]. In this field, ultrashort mid-IR pulses are beneficial because of their ability to provide large ponderomotive energy and to apply strong fields onto condensed matter without materials damage [100]. Here, nanoscale localization of an ultrashort-pulsed field enables coherent control of free-electron wavepackets and photocurrents on nanometer scale. The two fields that share common technologies of ultrafast mid-IR plasmonics may be developed into new coherent control schemes that treat both electronic and vibrational degrees of freedom at the mesoscopic scale.

The authors thank Fumiya Kusa, Akinobu Takegami, and Shingo Usui at Tokyo University of Agriculture and Technology and Atsunori Sakurai, Kei Murata, Kazuyuki Ishii, Kotaro Imasaka, Govind Dayal Singh, Shuta Kitade, and Nobuyoshi Hiramatsu at the University of Tokyo for their contributions to the presented works. The authors appreciate Claus Ropers, Georg Herink, Katharina Echternkamp, Lara Wimmer, and Murat Sivis at Göttingen University for the collaboration on the photoemission experiment described in Sect. 2.3 and for stimulating discussion on the relevant topics. S. A. acknowledges the support of Japan Society for the Promotion of Science (20H02651, 20K20556, 18K19030, 26600113) and Ministry of Education, Culture, Sports, Science and Technology (Q-LEAP JPMXS0118068681); I. M. acknowledges the support of Grants-in-Aid for JSPS Research Fellow (No. JP18J11212).

References

1. A.H. Zewail, Pure Appl. Chem. **72**, 2219 (2000)
2. S.A. Rice, Nature **409**, 422 (2001)
3. M. Shapiro, P. Brumer, Rep. Prog. Phys. **66**, 859 (2003)
4. B. Kohler, J.L. Krause, F. Raksi, K.R. Wilson, V.V. Yakovlev, R.M. Whitnell, Y. Yan, Acc. Chem. Res. **28**, 133 (1995)
5. R.J. Gordon, S.A. Rice, Annu. Rev. Phys. Chem. **48**, 601 (1997)
6. H. Rabitz, R. de Vivie-Riedle, M. Motzkus, K. Kompa, Science **288**, 824 (2000)
7. M.I. Stockman, S.V. Faleev, D.J. Bergman, Phys. Rev. Lett. **88**, 067402 (2002)
8. M. Aeschlimann, M. Bauer, D. Bayer, T. Brixner, F. J. GarcAa de Abajo, W. Pfeiffer, M. Rohmer, C. Spindler, F. Steeb: Nature **446**, 301 (2007)
9. P. Vasa, C. Ropers, R. Pomraenke, C. Lienau, Laser & Photon. Rev. **3**, 483 (2009)
10. M. Aeschlimann, M. Bauer, D. Bayer, T. Brixner, S. Cunovic, F. Dimler, A. Fischer, W. Pfeiffer, M. Rohmer, C. Schneider, F. Steeb, C. StrAŒber, D.V. Voronine, Proc. Nat. Acad. Sci. **107**, 5329 (2010)
11. S. Berweger, J.M. Atkin, X.G. Xu, R.L. Olmon, M.B. Raschke, Nano Lett. **11**, 4309 (2011)
12. D. Brinks, M. Castro-Lopez, R. Hildner, N.F. van Hulst, Proc. Nat. Acad. Sci. **110**, 18386 (2013)
13. M.D. Fayer, *Ultrafast Infrared Vibrational Spectroscopy* (CRC Press, 2013)
14. P. Hamm, M.T. Zanni, *Concepts and Methods of 2D Infrared Spectroscopy* (Cambridge University Press, 2011)
15. D. Laage, T. Elsaesser, J.T. Hynes, Chem. Rev. **117**, 10694 (2017)
16. A. Ghosh, J.S. Ostrander, M.T. Zanni, Chem. Rev. **117**, 10726 (2017)
17. J.C. Polanyi, Acc. Chem. Res. **5**, 161 (1972)

18. N. Doslić, K. Sundermann, L. González, O. Mó, J. Giraud-Girard, O. Kühn, Phys. Chem. Chem. Phys. **1**, 1249 (1999)
19. Y. Ohtsuki, M. Sugawara, H. Kono, Y. Fujimura, Bull. Chem. Soc. Jpn **74**, 1167 (2001)
20. M. Artamonov, T.S. Ho, H. Rabitz, Chem. Phys. **328**, 147 (2006)
21. C. Gollub, M. Kowalewski, S. Thallmaira, R. de Vivie-Riedle, Phys. Chem. Chem. Phys. **12**, 15780 (2010)
22. F. Kusa, S. Ashihara, J. Appl. Phys. **116**, 153103 (2014)
23. N. Hiramatsu, F. Kusa, K. Imasaka, I. Morichika, A. Takegami, S. Ashihara, J. Appl. Phys. **120**, 173103 (2016)
24. S. Usui, S. Kitade, I. Morichika, K. Kohmura, F. Kusa, S. Ashihara, J. Phys. Chem. C **121**, 26000 (2017)
25. F. Kusa, K.E. Echternkamp, G. Herink, C. Ropers, S. Ashihara, AIP Adv. **5**, 077138 (2015)
26. K. Imasaka, T. Kaji, T. Shimura, S. Ashihara, Opt. Express **26**, 21364 (2018)
27. F. Kusa, I. Morichika, A. Takegami, S. Ashihara, Opt. Express **25**, 12896 (2017)
28. I. Morichika, F. Kusa, A. Takegami, A. Sakurai, S. Ashihara, J. Phys. Chem. C **121**, 11643 (2017)
29. I. Morichika, K. Murata, A. Sakurai, K. Ishii, S. Ashihara, Nat. Commun. **10**, 3893 (2019)
30. R. Stanley, Nat. Photonics **6**, 409 (2012)
31. S. Law, V. Podolskiy, D. Wasserman, Nanophotonics **2**, 103 (2013)
32. Y. Zhong, S.D. Malagari, T. Hamilton, D. Wasserman, J. Nanophoton. **9**, 093791 (2015)
33. A. Hartstein, J.R. Kirtley, J.C. Tsang, Phys. Rev. Lett. **45**, 201 (1980)
34. F. Neubrech, A. Pucci, T.W. Cornelius, S. Karim, A. GarcAa-Etxarri, J. Aizpurua, Phys. Rev. Lett. **101**, 157403 (2008)
35. R. Adato, A. A. Yanik, J. J. Amsden, D. L. Kaplan, F. G. Omenetto, M. K. Hong, S. Erramilli, H. Altug: Proc. Nat. Acad. Sci. USA textbf106, 19227 (2009)
36. C.V. Hoang, M. Oyama, O. Saito, M. Aono, T. Nagao, Sci. Rep. **3**, 1175 (2013)
37. F. Neubrech, C. Huck, K. Weber, A. Pucci, H. Giessen, Chem. Rev. **117**, 5110 (2017)
38. X. Yang, Z. Sun, T. Low, H. Hu, X. Guo, F.J.G. de Abajo, P. Avouris, Q. Dai, Adv. Mater. **30**, 1704896 (2018)
39. R. Kas, O. Ayemoba, N.J. Firet, J. Middelkoop, W.A. Smith, A. Cuesta, Chem. Phys. Phys. Chem. **133**, 12881 (2019)
40. J. Cleary, R. Peale, D. Shelton, G. Boreman, R. Soref, W. Buchwald: MRS Proc. 1133-AA10-03 (2008)
41. A. Tittl, A. John-Herpin, A. Leitis, E.R. Arvelo, H. Altug, Angew. Chem. Int. Ed. **58**, 14810 (2019)
42. F. Kusunoki, J. Takahara, I. Kobayashi, Electron. Lett. **39**, 23 (2003)
43. T.W. Ebbesen, C. Genet, S.I. Bozhevolnyi, Phys. Today **61**, 44 (2008)
44. R. Soref, R.E. Peale, W. Buchwald, Opt. Express **16**, 6507 (2008)
45. R.L. Olmon, B. Slovick, T.W. Johnson, D. Shelton, S.-H. Oh, G.D. Boreman, M.B. Raschke, Phys. Rev. B **86**, 235147 (2012)
46. S. Law, L. Yu, D. Wasserman, J. Vac. Sci. Technol. B **31**, 03C121 (2013)
47. A.V. Zayats, Nature **495**, S7 (2013)
48. J. Zuloaga, P. Nordlander, Nano Lett. **11**, 1280 (2011)
49. P. Hommelhoff, Y. Sortais, A. Aghajani-Talesh, M.A. Kasevich, Phys. Rev. Lett. **96**, 077401 (2006)
50. C. Ropers, D.R. Solli, C.P. Schulz, C. Lienau, T. Elsaesser, Phys. Rev. Lett. **98**, 043907 (2007)
51. R. Bormann, M. Gulde, A. Weismann, S.V. Yalunin, C. Ropers, Phys. Rev. Lett. **105**, 147601 (2010)
52. M. Schenk, M. Kruger, P. Hommelhoff, Phys. Rev. Lett. **105**, 257601 (2010)
53. M. Krüger, M. Schenk, P. Hommelhoff, Nature **475**, 78 (2011)
54. G. Herink, D.R. Solli, M. Gulde, C. Ropers, Nature **483**, 190 (2012)
55. V. Schweikhard, A. Grubisic, T.A. Baker, D.J. Nesbitt, J. Phys. Chem. C **115**, 83 (2011)
56. A. Grubisic, V. Schweikhard, T.A. Baker, D.J. Nesbitt, Acs Nano **7**, 87 (2013)

57. P. Dombi, A. Horl, P. Racz, I. Marton, A. Trugler, J.R. Krenn, U. Hohenester, Nano Lett. **13**, 674 (2013)
58. S.M. Teichmann, P. Racz, M.F. Ciappina, J.A. Perez-Hernandez, A. Thai, J. Fekete, A.Y. Elezzabi, L. Veisz, J. Biegert, P. Dombi, Sci. Rep. **5**, 7584 (2015)
59. R.G. Hobbs, Y. Yang, A. Fallahi, P.D. Keathley, E. De Leo, F.X. Kartner, W.S. Graves, K.K. Berggren, Acs Nano **8**, 11474 (2014)
60. M. Gulde, S. Schweda, G. Storeck, M. Maiti, H.K. Yu, A.M. Wodtke, S. Schafer, C. Ropers, Science **345**, 200 (2014)
61. A. Mustonen, P. Beaud, E. Kirk, T. Feurer, S. Tsujino, Appl. Phys. Lett. **99**, 103504 (2011)
62. D.S. Yang, O.F. Mohammed, A.H. Zewail, Proc. Natl. Acad. Sci. U. S. A. **107**, 14993 (2010)
63. W.S. Graves, F.X. Kartner, D.E. Moncton, P. Piot, Phys. Rev. Lett. **108**, 263904 (2012)
64. L. Wimmer, G. Herink, D.R. Solli, S.V. Yalunin, K.E. Echternkamp, C. Ropers, Nat. Phys. **10**, 432 (2014)
65. M.I. Stockman, M.F. Kling, U. Kleineberg, F. Krausz, Nat. Photon. **1**, 539 (2007)
66. G. Herink, L. Wimmer, C. Ropers, New J. Phys. **16**, 123005 (2014)
67. M. Krüger, M. Schenk, M. Förster, P. Hommelhoff, J. Phys. B: At. Mol. Opt. Phys. **45**, 074006 (2012)
68. L.V. Keldysh, Sov. Phys. Jetp-Ussr. **20**, 1307 (1965)
69. R. H. Fowler, L. W. Nordheim: Proc. R. Soc. London, Ser **A119**, 173 (1928)
70. C.A. Spindt, I. Brodie, L. Humphrey, E.R. Westerberg, J. Appl. Phys. **47**, 5248 (1976)
71. G.G. Paulus, W. Becker, H. Walther, Phys Rev A **52**, 4043 (1995)
72. P. Alonso-Gonzalez, P. Albella, F. Neubrech, C. Huck, J. Chen, F. Golmar, F. Casanova, L.E. Hueso, A. Pucci, J. Aizpurua, R. Hillenbrand, Phys. Rev. Lett. **110**, 203902 (2013)
73. P.M. Donaldson, P. Hamm, Angew. Chem. Int. Ed. **52**, 634 (2013)
74. O. Selig, R. Siffels, Y.L.A. Rezus, Phys. Rev. Lett. **114**, 233004 (2015)
75. V.G. Kravets, A.V. Kabashin, W.L. Barnes, A.N. Grigorenko, Chem. Rev. **118**, 5912 (2018)
76. I. Morichika, F. Kusa, A. Takegami, and S. Ashihara: Proc. of SPIE **10252**, Optical Manipulation Conference, 1025215 (2017)
77. I. Morichika, A. Sakurai, S. Ashihara, EPJ Web of Conf. **205**, 03002 (2019)
78. J. Ma, Z. Qin, G. Xie, L. Qian, D. Tang, Appl. Phys. Rev. **6**, 021317 (2019)
79. D. Okazaki, H. Arai, A. Anisimov, E.I. Kauppinen, S. Chiashi, S. Maruyama, N. Saito, S. Ashihara, Opt. Lett. **44**, 1750 (2019)
80. D. Okazaki, I. Morichika, H. Arai, E.I. Kauppinen, Q. Zhang, A. Anisimov, I. Varjos, S. Chiashi, S. Maruyama, S. Ashihara, Opt. Express **28**, 19997 (2020)
81. J.P. Kraack, P. Hamm, Chem. Rev. **117**, 10623 (2017)
82. M.K. Petti, J.S. Ostrander, V. Saraswat, E.R. Birdsall, K.L. Rich, J.P. Lomont, M.S. Arnold, M.T. Zanni, J. Chem. Phys. **150**, 024707 (2019)
83. Y. Yang, C. Gu, J. Li, Small **15**, e1804177 (2019)
84. B. Cohn, B. Engelman, A. Goldner, L. Chuntonov, J. Phys. Chem. Lett. **9**, 4596 (2018)
85. R.T. Mackin, B. Cohn, B. Engelman, A. Goldner, I.V. Rubtsov, L. Chuntonov, J. Phys. Chem. C **123**, 24731 (2019)
86. K. Heyne, O. Kuhn, J. Am. Chem. Soc. **141**, 11730 (2019)
87. L. Windhorn, T. Witte, J.S. Yeston, D. Proch, M. Motzkus, K.L. Kompa, W. Fuss, Chem. Phys. Lett. **357**, 85 (2002)
88. L. Windhorn, J.S. Yeston, T. Witte, W. Fuss, M. Motzkus, D. Proch, K.-L. Kompa, C.B. Moore, J. Chem. Phys. **119**, 641 (2003)
89. T. Witte, T. Hornung, L. Windhorn, D. Proch, R. de Vivie-Riedle, M. Motzkus, K.L. Kompa, J. Chem. Phys. **118**, 2021 (2003)
90. V.D. Kleiman, S.M. Arrivo, J.S. Melinger, E.J. Heilweil, Chem. Phys. **233**, 207 (1998)
91. T. Witte, J.S. Yeston, M. Motzkus, E.J. Heilweil, K.L. Kompa, Chem. Phys. Lett. **392**, 156 (2003)
92. C. Ventalon, J.M. Fraser, M.H. Vos, A. Alexandrou, J.L. Martin, M. Joffre, Proc. Nat. Ac. Sci. **101**, 13216 (2004)
93. D.B. Strasfeld, S.H. Shim, M.T. Zanni, Phys. Rev. Lett. **99**, 038102 (2007)

94. T. Stensitzki, Y. Yang, V. Kozich, A.A. Ahmed, F. Kössl, O. Kühn, K. Heyne, Nat. Chem. **10**, 126 (2018)
95. M. Delor, S.A. Archer, T. Keane, A.J.H.M. Meijer, I.V. Sazanovich, G.M. Greetham, M. Towrie, J.A. Weinstein, Nat. Chem. **9**, 1099 (2017)
96. A.N. Grigorenko, M. Polini, K.S. Novoselov, Nat. Photon. **6**, 749 (2012)
97. G.X. Ni, A.S. McLeod, Z. Sun, L. Wang, L. Xiong, K.W. Post, S.S. Sunku, B.-Y. Jiang, J. Hone, C.R. Dean, M.M. Fogler, D.N. Basov, Nature **557**, 530 (2018)
98. M.F. Ciappina et al., Rep. Prog. Phys. **80**, 054401 (2017)
99. P. Dombi et al., Rev. Mod. Phys. **92**, 025003 (2020)
100. S. Ghimire, D.A. Reis, Nat. Phys. **15**, 10 (2019)